Small-scale magnetic actuators with optimal six degrees-of-freedom

Changyu Xu, Zilin Yang, Guo Zhan Lum*

Nanyang Technological University, School of Mechanical and Aerospace Engineering, 50 Nanyang Avenue, Singapore 639798

*Correspondence to: gzlum@ntu.edu.sg

Abstract

Magnetic miniature robots (MMRs) are small-scale, untethered actuators which can be controlled by magnetic fields. As these actuators can non-invasively access highly confined and enclosed spaces, they have great potential to revolutionize numerous applications in robotics, materials science and biomedicine. While the creation of MMRs with six-degrees-of-freedom (six-DOF) represents a major advancement for this class of actuators, these robots are not widely adopted due to two critical limitations: (i) under precise orientation control, these MMRs have slow sixth-DOF angular velocities (4 degree/second) and it is difficult to apply desired magnetic forces on them; (ii) such MMRs cannot perform soft-bodied functionalities. Here we introduce a fabrication method that can magnetize optimal MMRs to produce 51–297 folds larger sixth-DOF torque than existing small-scale, magnetic actuators. We also propose a universal actuation method that is applicable for rigid and soft MMRs with six-DOF. Under precise orientation control, our optimal MMRs could execute full six-DOF motions reliably and achieve sixth-DOF angular velocities of 173 degree/second. Our soft MMRs could display unprecedented functionalities; our six-DOF jellyfish-like robot could swim across barriers impassable by existing similar devices and our six-DOF gripper was 20 folds quicker than its five-DOF predecessor in completing a complicated, small-scale assembly.

Keywords: Magnetic materials; actuators; miniature robots; soft robots; locomotion; small-scale assembly

Introduction

Miniature robots are untethered actuators that are in the millimeter scale or smaller. A unique characteristic of such actuators is that their size and mobility allow them to non-invasively access highly confined and enclosed spaces to perform a wide range of micro/nano-manipulation tasks (1). Due to this ability, miniature robots have the potential to create a paradigm shift for medical treatments like minimally-invasive surgery and targeted drug delivery (2-8). In addition to such applications, these robots have also proven to be very useful in facilitating a broad range of fundamental studies for materials science (9-11) and biology (12-19), as well as enabling numerous types of unprecedented lab-on-chip applications (20-23).

Among the miniature robots, the magnetically actuated ones are especially effective to operate in enclosed spaces because their actuating signals, in the form of remote magnetic fields, can easily and harmlessly penetrate through most biological and synthetic materials (6, 24-48). Furthermore, magnetic actuation offers more control parameters over other actuation methods (e.g., heat, chemicals, pressure (9)), because the actuating magnetic fields can be specified not only in their magnitude but also in their directions and spatial-gradients (9, 30, 37, 38). Due to this unique advantage, magnetic miniature robots (MMRs) have shown to be more mobile and functional among the small-scale, untethered actuators (38, 39).

Orientation control is very critical for MMRs because it dictates their positioning and manipulation performances (30, 39). Hence, the creation of MMRs, which have six degrees-of-freedom (DOF) rigid-body motions, is a major advancement for this class of actuators as the highly sought-after sixth-DOF rotation about their net magnetic moment was previously unattainable (49, 50). By enabling the sixth-DOF rotation, the capabilities of six-DOF MMRs can possibly be much higher than their traditional five-DOF counterparts, which can only translate along three axes and rotate about two axes (30). For instance, if six-DOF MMRs can replace their five-DOF counterparts in (10, 11, 20, 22), these robots will be able to pick-and-place miniature objects in a much more efficient

manner, potentially accelerating the process of assembling these objects into their desired planar (11) or 3D configurations (10, 20, 22). Likewise, while the soft MMRs in (38, 39) are able to perform dexterous locomotion, they are still controlled via the traditional five-DOF actuation. If such MMRs are able to rotate about their sixth-DOF axis, their dexterity can hypothetically be enhanced substantially, allowing them to better negotiate across unstructured environments.

While six-DOF MMRs have considerable potential (49-52), it remains an open challenge to control such actuators effectively. In recent developments, Petruska has shown that six-DOF MMRs are able to implement precise orientation control via using dynamic magnetic fields (52). This is a substantial improvement for six-DOF MMRs since such actuators were previously unable to control their orientation precisely (49-51). Nonetheless, there still exist several limitations in the actuation method developed by Petruska (52). For example, the achievable sixth-DOF angular velocities by their MMRs are limited to 4 degree/second (52). Furthermore, as the net magnetic moment of their MMRs is changing dynamically when they are under precise orientation control, it will be difficult to determine the required magnetic spatial-gradients to translate these actuators with desired magnetic forces (52). The actuation method of Petruska is also only applicable for MMRs with soft magnetic properties (52). Since MMRs with hard magnetic properties will not be easily re-magnetized (24, 53, 54), such actuators will be more deterministic than their counterparts with soft magnetic properties. Therefore, it will be beneficial if precise orientation control can also be implemented for six-DOF MMRs with hard magnetic properties. In addition to these challenges, existing six-DOF MMRs are also restricted to rigid bodies, and thus they are unable to deform and generate soft-bodied mechanical functionalities (49-52). It will be highly desirable to endow these actuators with soft-bodied functionalities because this can potentially enable them to generate a series of time-varying deformations to execute dexterous locomotion and realize critical mechanical functions such as active gripping (7, 10, 38, 39). Due to the limitations of existing six-DOF MMRs, these actuators are not widely adopted. Except for the works in (49-52), all the MMRs are still designed for the traditional five-DOF actuation (e.g., (36, 38, 39, 54-68)).

Here we present a fabrication method that can exactly magnetize and construct the optimal actuator/robot design reported by Diller et al. (50). Using this optimal design, our MMRs will be able to maximize their sixth-DOF torque without compromising the actuation capabilities of their remaining five-DOF. While the optimal actuator design has been proposed by Diller et al. (50), the construction of such sophisticated MMRs remains an open challenge in the literature. It is critical to create such optimal MMRs because the achievable sixth-DOF torque of existing actuators is substantially weaker than their magnetic torques generated about the other two axes (49-51). As an example, the maximum sixth-DOF torque producible by the MMR of Giltinan and Sitti is computed to be 6984 folds weaker than the maximum magnetic torques achievable by the other two axes (51) (supplementary information (SI) section S1D). To enhance the capabilities of six-DOF MMRs, it is therefore essential to significantly increase the strength of their sixth-DOF torque. In addition, we also introduce a universal actuation method that can be applied to six-DOF MMRs with rigid or deformable soft bodies, and actuators with hard or soft magnetic properties. The proposed actuation method can implement precise orientation control on our optimal MMRs while allowing them to execute full six-DOF motions reliably and achieve high sixth-DOF angular velocities. Based on our proposed fabrication and actuation methods, we can resolve all the critical challenges of six-DOF MMRs, and empower these actuators to be practical and functional across a broad range of applications.

Fabrication Method

Here we propose a fabrication method that can magnetize and construct the optimal robot design reported by Diller et al. (50). The body of this optimal six-DOF MMR can be divided into two components (Fig. 1A(i)): (i) a main component that possesses a non-uniform magnetization profile ($\vec{M}_m$), which will produce zero net magnetic moment (Fig. 1A(ii)). This magnetization profile can be approximated as a distribution of magnetic dipoles in the main component (38). (ii) a uniformly magnetized auxiliary magnet of which

its main function is to offer a net magnetic moment ($\vec{m}$) to the robot. When the magnetization profiles of the main component and the auxiliary magnet are considered as a whole, they form the resultant magnetization profile of the robot ($\vec{M}$), and the sixth-DOF rotational axis would be the axis about the robot's $\vec{m}$ (Fig. 1A(i)). The main component is the key constituent of this optimal MMR because while the auxiliary magnet facilitates the traditional five-DOF rigid-body motions of the robot, the highly sought-after sixth-DOF rotation can only be enabled by the main component (49, 50). In theory, the robot's net magnetic moment ($\vec{m}$) has no effects on the sixth-DOF torque, but increasing its magnitude will linearly enhance the producible three-axes of magnetic forces and magnetic torques about the other two axes (49, 50). Conversely, the main component will dictate the maximum producible sixth-DOF torque of the robot, but its design will not affect the actuation on the robot's remaining five-DOF motions (49, 50).

A significant advantage of the optimal MMR is that it can produce much higher sixth-DOF torques than the existing six-DOF robots presented in (49-51), while possessing the same actuation abilities in the traditional five-DOF as them. For instance, an optimal MMR that has a footprint of 4 mm diameter and 2 mm out-of-plane thickness, $|\vec{m}|$ of 0.64 $\mu\mathrm{Am}^2$ and $|\vec{M}|$ of 19334 $\mathrm{A/m}$, will be able to produce a *normalized** sixth-DOF torque (per Tesla/meter) of $6.48 \times 10^{-7}\mathrm{Nm}^2/\mathrm{T}$ (SI section S2A). This amount of torque is 297 folds larger than the achievable sixth-DOF torque by the MMRs of Diller et al. (49, 50), where their actuators with the same footprint, $|\vec{m}|^{\dagger}$ and $|\vec{M}|$ can only produce a normalized sixth-DOF torque of $2.18 \times 10^{-9}\,\mathrm{Nm}^2/\mathrm{T}$ (SI section S1D). Similarly, an optimal six-DOF MMR that has the same footprint, $|\vec{m}|$ and $|\vec{M}|$ as the robot of Giltinan and Sitti (51), will

* The robots' sixth-DOF torque has been normalized according to the strength of the actuating signals so that a fairer comparison can be made between different robots and also across different magnetic actuation systems. Robots with higher normalized sixth-DOF torque will be able to generate higher restoring torques about this axis.

† Robots with equal $|\vec{m}|$ have the same actuation abilities for their traditional five-DOF (49, 50)

be able to produce 51 folds higher normalized sixth-DOF torque (SI section S1D and SI section S2A).

The actuator design in Fig. 1A is optimal because its $\vec{M}_m$ is designed to maximize the robot's sixth-DOF torque while ensuring that the robot's sixth-DOF rotation will be decoupled with its translation (see SI section S1E for the mathematical proof). The sixth-DOF torque is essentially a rigid-body torque that is induced by the distributed magnetic forces on the robot's body. Due to the specified $\vec{M}_m$, the applied magnetic forces across all the points on the main component are always maximized and perpendicular to their corresponding moment arms from the robot's sixth-DOF axis (50). Hence, this will in turn maximize the cross product of the distributed forces and moment arms, enabling the generated sixth-DOF torque to be optimized (50). The proof in SI section S1E dictates that $\vec{M}_m$ is optimal and unique, and this is established by analyzing the robot's normalized sixth-DOF torque via its local reference frame. Because this proof is derived independently from the configuration of magnetic actuation systems (e.g., the described electromagnetic coil system in Methods section B), it will hold true for all systems.

The construction of the optimal six-DOF MMR remains an open challenge because it is very difficult to magnetize the highly complex $\vec{M}_m$ within the main component (Fig. 1A(ii)). To construct this component, here we first exploit the symmetrical features of $\vec{M}_m$ to divide its body into four identical quadrants. Standard 3D-printing polymers are used to create corresponding molds for the quadrants. Each quadrant is then molded with a soft polymer matrix (Ecoflex 00-10 (Smooth-on, Inc)), which has embedded NdFeB magnetic particles (average size of 5 μm (MQFP; Magnequench)). The NdFeB particles are mixed uniformly within the polymer matrix and the quadrants will be cured in an 80°C oven after two hours (see Methods section A for more details).

To program the desired magnetization profile into each quadrant, the quadrants are first deformed into semi-circles with polymer jigs constructed by 3D-printing. In their deformed configuration, the quadrants are subsequently magnetized by a strong, uniform magnetic field (Fig. 1B(i)-(iii) and Methods section A). Once a quadrant recovers to its original

shape, it will possess the exact optimal magnetization profile (Fig. 1B(iv) and see SI section S2B for the mathematical proof). The main component can be formed once four of such magnetized quadrants are adhesively bonded together (Fig. 1B(v)). Since this magnetization method is able to exactly create the optimal $\vec{M}_m$ for the main component (Fig. 1B(vi)), the construction for the optimal six-DOF MMRs can now become practical. If the main component has to be made smaller, an at-scale main component can be cut out from the center of the original piece. As an example, we have illustrated the cut-out piece as a cylinder (Fig. 1B(vi)), because such a shape can be more easily carved via mechanical means in practice. If it is necessary to construct a long cylindrical main component, such a component can be constructed via stacking, aligning and bonding several short cylindrical main components together. In general, main components with any arbitrary shape can also be obtained if the cut-out process in Fig. 1B(vi) is implemented by the laser machining techniques shown in (38, 39). As $\vec{M}_m$ is identical along the radial lines (Fig. 1B(vi)), no matter what shape the cut-out piece possesses, it can always fully inherit this profile to enable the robot's sixth-DOF torque to be maximized. In the future, we will aim to further investigate the geometrical effects and optimal shape of the main component. It is also noteworthy that our fabrication method is only applicable for main component with hard magnetic properties. We will explore expanding such fabrication methods to construct main component with soft magnetic properties in the future.

In general, the shape of the auxiliary magnet can be optimized accordingly to suit different applications. The auxiliary magnet also does not need to be rigid and it can be replaced by active soft components as long as these components can provide a net magnetic moment for the six-DOF MMRs. For instance, we can endow our optimal MMRs with active soft components to enable them to perform dexterous soft-bodied locomotion and active gripping. For simplicity purposes, we will illustrate the proposed fabrication method with a rigid auxiliary magnet that has a 3D triangular shape. Such a component can be constructed via molding a polymer matrix (PDMS (Dow Corning)), which has embedded NdFeB magnetic particles (average size of 5 μm (MQFP; Magnequench)). Similar to the main component, these embedded NdFeB particles are mixed uniformly within the polymer matrix and the auxiliary magnet will be cured in an 80°C oven after two hours.

Once molded, the auxiliary magnet is magnetized uniformly by a strong magnetic field, and the construction of the optimal six-DOF MMR will be completed after the auxiliary magnet is adhesively bonded to the main component (Fig. 1B(vii), please also see Methods section A for more information).

Actuation Method

Our proposed method is to control the actuating magnetic signals under quasi-static conditions such that a six-DOF MMR will constantly experience three axes of restoring torques. Under the influence of the restoring torques, the robot's three axes of angular displacements will self-align into their respective desired angles (Fig. 1C). While the six-DOF MMR will be in a rotational equilibrium state when its angular displacements reach the desired angles, the presence of the restoring torques enables the robot to maintain this desired orientation as they can reject external torque disturbances that tend to misalign it. To facilitate our subsequent discussions, we shall define the desired orientation (i.e., the rotational equilibrium state) as the minimum potential energy configuration.

Our proposed actuation method is universal and therefore it is applicable not only to our optimal robots but also across all types of six-DOF MMRs with rigid or soft bodies, and with hard or soft magnetic properties. While the conditions for making the robot's desired orientation into a minimum potential energy configuration can be derived via either the Newton-Euler or the energy methods, the former method is selected here as it is more intuitive for describing the restoring torques. In our analysis, we will also include two practical constraints: (i) the magnetic actuating signals are assumed to be uniform across the robot's body as it is difficult to make such signals spatially-invariant at small-scales (1, 9, 30); (ii) due to the constraints of the Gauss's law and the Ampere's law (SI section S1A), there are only five independent spatial-gradients for the time-varying magnetic field ($\vec{B}$). To aid our subsequent derivations, we will represent the independent spatial gradients of $\vec{B}$ with the time-varying vector $\vec{B}_{\text{grad}}$, and the explicit representations for $\vec{B}$ and $\vec{B}_{\text{grad}}$ are given as:

$$\vec{B} = [B_x \quad B_y \quad B_z]^{\mathrm{T}}, \qquad \vec{B}_{\mathrm{grad}} = \left[\frac{\partial B_z}{\partial x} \quad \frac{\partial B_z}{\partial y} \quad \frac{\partial B_z}{\partial z} \quad \frac{\partial B_y}{\partial y} \quad \frac{\partial B_x}{\partial y}\right]^{\mathrm{T}}, \tag{1}$$

where B_x, B_y and B_z represent the Cartesian x-, y- and z-components of $\vec{B}$, respectively.

By having a non-uniform magnetization profile ($\vec{M}$), a six-DOF MMR will experience an external wrench when $\vec{B}$ and $\vec{B}_{\mathrm{grad}}$ are applied. These effects can be best analyzed with a local reference frame, which has one of its principal axes parallel to the robot's net magnetic moment ($\vec{m}$), i.e., its sixth-DOF rotational axis (49, 50). The robot's net magnetic moment can be computed as $\vec{m} = \iiint \vec{M}\ \mathrm{d}V$, where V represents the volume of the robot. Here we use the z-axis of the local reference frame to represent the sixth-DOF rotational axis of the robot (Fig. 1D(iii)). Based on this local reference frame, the net magnetic torque, $\vec{\tau}$, and magnetic force, $\vec{F}$, experienced by the robot can be expressed as (49, 50):

$$\begin{pmatrix} \vec{\tau}_{\{L\}} \\ \vec{F}_{\{L\}} \end{pmatrix} = \begin{pmatrix} \vec{m}_{\{L\}} \times \vec{B}_{\{L\}} + \iiint \vec{r}_{\{L\}} \times \left(\left[\frac{\partial \vec{B}_{\{L\}}}{\partial x_{\{L\}}} \quad \frac{\partial \vec{B}_{\{L\}}}{\partial y_{\{L\}}} \quad \frac{\partial \vec{B}_{\{L\}}}{\partial z_{\{L\}}} \right]^{\mathrm{T}} \vec{M}_{\{L\}} \right) \mathrm{d}V \\ \left(\vec{m}_{\{L\}} \cdot \nabla\right) \vec{B}_{\{L\}} \end{pmatrix}$$

$$= \mathbf{D} \begin{pmatrix} \vec{B}_{\{L\}} \\ \vec{B}_{\mathrm{grad},\{L\}} \end{pmatrix}, \tag{2}$$

where $\vec{r}$ represents the displacement vector from the robot's center of mass to a given point on the robot body. The subscript $\{L\}$ indicates that the analysis is performed according to the local reference frame. The matrix **D** is known as the 6×8 design matrix (49, 50), and its elements are dependent on the robot's geometry and magnetization profile (see SI section S1C for the derivation of Eq. (2)). For the robot to possess six-DOF under quasi-static actuation, its **D** matrix must be full ranked and this requirement is true regardless if the robot has hard or soft magnetic properties (49, 50).

Although the local reference frame is intuitive for analyzing and designing six-DOF MMRs (49, 50), this reference frame does not encompass the information of the robot's sixth-DOF

angular displacement. As a result, it will be difficult to make a six-DOF robot's desired orientation into a minimum potential energy configuration according to this reference frame. Hence, we introduce an intermediate reference frame to reanalyze Eq. (2) (Fig. 1D(ii)). All the analyses that are performed in this reference frame will be denoted with the subscript $\{I\}$, and the mathematical relationship between the vectors in the intermediate and local reference frames is given as:

$$\vec{v}_{\{I\}} = \mathbf{R}_z(\theta)\vec{v}_{\{L\}}, \tag{3}$$

where $\mathbf{R}_z$ is the standard rotational matrix about the z-axis (SI section S3A) and θ represents the desired sixth-DOF angular displacement. The vector $\vec{v}$ in Eq. (3) can be any arbitrary vector, including displacement vectors, $\vec{\tau}$, $\vec{F}$ and $\vec{B}$. Based on Eq. (3), the local reference frame $\vec{B}$ and $\vec{B}_{\text{grad}}$ can be converted into the intermediate reference frame via the following mapping:

$$\begin{pmatrix} \vec{B}_{\{L\}} \\ \vec{B}_{\text{grad},\{L\}} \end{pmatrix} = \mathbf{A} \begin{pmatrix} \vec{B}_{\{I\}} \\ \vec{B}_{\text{grad},\{I\}} \end{pmatrix},$$

$$\text{where} \quad \mathbf{A} = \begin{bmatrix} \mathbf{R}_z(\theta)^{\mathrm{T}} & \mathbf{0}_{3\times5} \\ \mathbf{0}_{5\times3} & \mathbf{A}_1(\theta) \end{bmatrix}, \tag{4}$$

and $\mathbf{A_1}$ is a matrix that can be derived via the chain rule and Eq. (3) (SI section S3A). The matrices $\mathbf{0}_{3\times5}$ and $\mathbf{0}_{5\times3}$ are 3×5 and 5×3 zero matrices, respectively. Using Eq.s (3) and (4), we can reanalyze Eq. (2) with the intermediate reference frame via the following mapping:

$$\begin{pmatrix} \vec{\tau}_{\{I\}} \\ \vec{F}_{\{I\}} \end{pmatrix} = \begin{pmatrix} \mathbf{R_z}(\theta) & \mathbf{0}_{3\times3} \\ \mathbf{0}_{3\times3} & \mathbf{R_z}(\theta) \end{pmatrix} \begin{pmatrix} \vec{\tau}_{\{L\}} \\ \vec{F}_{\{L\}} \end{pmatrix}$$

$$= \begin{pmatrix} \mathbf{R_z}(\theta) & \mathbf{0}_{3\times3} \\ \mathbf{0}_{3\times3} & \mathbf{R_z}(\theta) \end{pmatrix} [\mathbf{D}] \begin{pmatrix} \vec{B}_{\{L\}} \\ \vec{B}_{\text{grad},\{L\}} \end{pmatrix}$$

$$= \begin{pmatrix} \mathbf{R_z}(\theta) & \mathbf{0}_{3\times3} \\ \mathbf{0}_{3\times3} & \mathbf{R_z}(\theta) \end{pmatrix} [\mathbf{D}][\mathbf{A}(\theta)] \begin{pmatrix} \vec{B}_{\{I\}} \\ \vec{B}_{\text{grad},\{I\}} \end{pmatrix}$$

$$= [\mathbf{C}(\theta)] \begin{pmatrix} \vec{B}_{\{I\}} \\ \vec{B}_{\text{grad},\{I\}} \end{pmatrix},$$

$$\text{where } \mathbf{C}(\theta) = \begin{pmatrix} \mathbf{R_z}(\theta) & \mathbf{0}_{3\times3} \\ \mathbf{0}_{3\times3} & \mathbf{R_z}(\theta) \end{pmatrix} [\mathbf{D}][\mathbf{A}(\theta)], \tag{5}$$

and $\mathbf{0}_{3\times3}$ is a 3×3 zero matrix. We define $\mathbf{C}$ to be the control matrix, and it is a full-ranked 6×8 matrix when the rank of $\mathbf{D}$ is full (see SI section S3A for the explicit representation of $\mathbf{C}$).

To make the desired orientation of the robot into a minimum potential energy configuration, we specify $\vec{\tau}_{\{I\}}$ in Eq. (5) to be a null vector at the desired θ. While the robot experiences zero torque at the desired orientation, a magnetic force $\vec{F}_{\{I\}}$ can still be specified for the robot. This is a significant advantage over the actuation method developed by Petruska (52), as our proposed method can translate the six-DOF MMRs with desired magnetic forces when they are under precise orientation control. Based on the desired $\vec{F}_{\{I\}}$, the required actuating magnetic signals of our proposed method can be obtained by solving Eq. (5):

$$\begin{pmatrix} \vec{B}_{\{I\}} \\ \vec{B}_{\text{grad},\{I\}} \end{pmatrix} = \mathbf{C}^{\mathrm{T}}[\mathbf{C}\mathbf{C}^{\mathrm{T}}]^{-1} \begin{pmatrix} \vec{0}_{3\times1,\{I\}} \\ \vec{F}_{\{I\}} \end{pmatrix} + k_1 \begin{pmatrix} 0 \\ 0 \\ 1 \\ 0 \\ 0 \\ 0 \\ 0 \end{pmatrix}_{\{I\}} + k_2 \begin{pmatrix} \dfrac{(d_5 d_{14} - d_4 d_{15})\sin\theta - (d_4 d_{14} + d_5 d_{15})\cos\theta}{(d_{15}\cos 2\theta - d_{14}\sin 2\theta)m} \\ \dfrac{(d_4 d_{15} - d_5 d_{14})\cos\theta - (d_4 d_{14} + d_5 d_{15})\sin\theta}{(d_{15}\cos 2\theta - d_{14}\sin 2\theta)m} \\ 0 \\ 0 \\ 0 \\ 0 \\ 1 \\ -\dfrac{d_{14}\cos 2\theta + d_{15}\sin 2\theta}{d_{15}\cos 2\theta - d_{14}\sin 2\theta} \end{pmatrix}_{\{I\}}. \tag{6}$$

Equation (6) presents the general solution of our actuating magnetic fields. Unlike previous actuation methods for six-DOF MMRs (49-52), this closed-form solution can now fully explain the actuation principles of such robots under quasi-static conditions and enable us

to execute effective six-DOF control on them. The first right-hand component represents the particular solution obtained via pseudo-inverse, while the other two vectors on the right are the null space vectors of $\mathbf{C}$ and they represent the homogeneous solutions. The scalar variables k_1 and k_2 are the scale factors of the null space vectors. The variables d_4, d_5, d_{14} and d_{15} are the elements of $\mathbf{D}$ (see SI section S1C for their detail representations), and m represents the magnitude of $\vec{m}$.

The pseudo-inverse solution in Eq. (6) ensures that the robot will be in a rotational equilibrium state when it reaches the desired orientation (i.e., minimum potential energy configuration), and also that the desired $\vec{F}_{\{I\}}$ can be applied to the robot. This solution, however, is unable to tune the actuating signals such that we can control the restoring torques applied to the robot. The restoring torques can instead be controlled by tuning the actuating signals via the homogeneous solutions.

The first null space vector in Eq. (6), $(0\ \ 0\ \ 1\ \ 0\ \ 0\ \ 0\ \ 0\ \ 0)_{\{I\}}{}^{\mathrm{T}}$, adjusts $\vec{B}$ such that it can become stronger along its z-axis component, i.e., this vector is used for increasing $B_{z,\{I\}}$. Increasing the magnitude of $B_{z,\{I\}}$ is critical because it increases the restoring torque that aligns the robot's $\vec{m}$ to its desired direction (49, 50). A stronger restoring torque is ideal because it empowers the robot to reject torque disturbances more effectively. Despite this ability, this null space vector can only generate two axes of restoring torques for the robot and it has no effects on the robot's sixth-DOF rotation (30, 49, 50).

Unlike the pseudo-inverse solution and the first null space vector, the existence of the second null space vector in Eq. (6) has never been revealed in the literature. Here we discover that the second null space vector has great significance for actuating MMRs because it holds the key for generating their sixth-DOF restoring torque (SI section S3B). By adjusting the magnetic actuating signals in Eq. (6) via this null space vector, we can now command the robot's sixth-DOF angular displacement to self-align into its desired θ and subsequently maintain this angle. A critical requirement for enabling the sixth-DOF restoring torque is to determine the correct range of k_2, and such detailed discussions can be found in SI section S3B.

The general solution in Eq. (6) can be applied to six-DOF MMRs with rigid or soft deformable bodies. In comparison, it will be easier to actuate six-DOF MMRs with rigid bodies because their null space vectors in Eq. (6) will not change due to them having mechanical deformations. However, their soft counterparts have to be designed in such a way that the directions of their null space vectors in Eq. (6) will remain constant when they undergo a series of time-varying deformations. A potential method to realize this requirement is to make the magnetization and stiffness profiles of the robots rotary symmetrical about the sixth-DOF axis, and only allow these actuators to execute their time-varying deformations via adjusting the magnitude of the first null space vector in Eq. (6). Indeed, this method has been proven effective when we actuate various six-DOF MMRs with soft-bodied functionalities (Experimental Results section).

In theory, it will be ideal for the magnitudes of k_1 and k_2 in Eq. (6) to approach infinity as this can enable the strength of the restoring torques in all three axes to become infinite. However, as the magnitudes of k_1 and k_2 are in practice constrained by the capacity of the magnetic actuation systems (e.g., the described electromagnetic coil system in Methods section B), the strength of the restoring torques becomes highly dependent on the robot's design (i.e., its **D** matrix). The best design that can complement our actuation method will be the optimal design in Fig. 1A because such MMRs will be able to maximize their sixth-DOF restoring torque in any given magnetic actuation system. Regardless of the six-DOF robot's design, the magnetic actuating signals in Eq. (6) should always be computed with the highest permissible magnitudes of k_1 and k_2 as this can maximize the robot's restoring torques. Because the actuating signals have to be eventually specified according to a global reference frame (30, 49, 50), the computed $\vec{B}_{\{I\}}$ and $\vec{B}_{\text{grad},\{I\}}$ in Eq. (6) will be mapped into this reference frame (Fig. 1D(i)):

$$\begin{pmatrix} \vec{B}_{\{G\}} \\ \vec{B}_{\text{grad},\{G\}} \end{pmatrix} = \begin{bmatrix} \mathbf{R}_x(\alpha)\mathbf{R}_y(\beta) & \mathbf{0}_{3\times5} \\ \mathbf{0}_{5\times3} & \mathbf{A}_2(\alpha,\beta) \end{bmatrix} \begin{pmatrix} \vec{B}_{\{I\}} \\ \vec{B}_{\text{grad},\{I\}} \end{pmatrix}, \tag{7}$$

where $\mathbf{R}_x$ and $\mathbf{R}_y$ are the standard x- and y-axis rotational matrices (SI section S3A), and the detailed derivation of $\mathbf{A}_2$ can be found in SI section S3A. The variables α and β

represent the corresponding desired angular displacement about these axes, and together they define the intermediate reference frame as well as the desired orientation for $\vec{m}$ (Fig. 1D(i)-(ii)). The subscript $\{G\}$ in Eq. (7) indicates that the vectors are expressed in the global reference frame. Equation (7) concludes our proposed actuation method as it shows how we can specify the required actuating signals, according to the global reference frame, to make the robot's desired orientation into a minimum potential energy configuration. Using the proposed actuation method, six-DOF MMRs can also be controlled to follow a given angular trajectory. This can be achieved by breaking the trajectory into a sequence of discrete angular displacements, and sequentially make all these orientations into a minimum potential energy configuration. If necessary, desired magnetic forces can also be applied on the MMRs at any point of the angular trajectory so that these actuators can fully utilize their six-DOF motions.

Experimental Results

As a proof-of-concept, we first provided a qualitative, visual demonstration for our proposed fabrication method. We carried out the procedures in Fig. 1B(i)-(v) to construct a centimeter-scale main component, and the magnetization process in Fig. 1B(iii) was simulated by printing horizontal arrows onto the deformed quadrants (Fig. 2A(i)). Once the quadrants were released from their deformed state (Fig. 2A(ii)) and bonded together as a main component (Fig. 2A(iii)), it could be observed from the printed arrows that the main component was able to produce a similar magnetization profile that was specified in Fig. 1A(ii).

To provide a quantitative evaluation for the proposed fabrication method of the main component, we fabricated a main component of 3 mm diameter and 1 mm out-of-plane thickness, and attached it to the free-end of a fixed-free beam (Fig. 2B(i)). This beam was used in the experiment for establishing the relationship between the magnitude of the sixth-DOF torque and the applied magnetic actuating signals (according to the local reference frame). As the beam would deform when we applied a sixth-DOF torque onto the main component, we could visually measure the angular deformation on the beam's free-end

(θ_{tip}) from the camera, and used the Euler-Bernoulli equation to deduce the applied sixth-DOF torque (SI section S4A). In theory, the applied sixth-DOF torque on the main component would deform the beam by inducing a constant bending moment along its body, and the magnitudes of the bending moment and sixth-DOF torque would be equal. The experimental results obtained from this method were plotted in Fig. 2B(ii) where the x- and y-axes of the plot represented the applied magnetic actuating signals and sixth-DOF torque, respectively. Each data point in the plot was evaluated with five trials, and a best fit line was plotted based on these data points. The gradient of the best fit line represented the main component's producible normalized sixth-DOF torque, and this value was computed to be 4.20×10^{-7} Nm^2/T. This experimental value had only 7% deviation from the theoretical normalized sixth-DOF torque, which was predicted to be 3.95×10^{-7} Nm^2/T (SI section S2A). These experiment results therefore agreed with our theory, suggesting that the proposed fabrication method was indeed able to magnetize and construct the main component of the optimal six-DOF MMR. The small deviation between the experiments and theory could be contributed by minor fabrication errors of the beam and main component, as well as the visual measurement errors from the camera.

Next, we proceeded to build various optimal six-DOF MMRs. As robots with hard magnetic properties were more deterministic than their counterparts with soft magnetic properties (24, 53, 54), we had endowed all our constructed miniature robots with hard magnetic properties. We first built the optimal six-DOF MMR specified in Fig. 1A and we used this rigid robot to evaluate the effectiveness of our proposed actuation method. This millimeter-scale robot was shown to be able to execute all its six-DOF rigid-body motions well regardless if it was in contact with the substrate or within the fluid bulk (SI Video S1). When the robot was in contact with the passive substrate (Fig. 2C), its motions were resisted by the frictional forces and torques induced from the substrate. To make the robot motions smoother, we had reduced the frictional effects by applying an upward magnetic force (1.29×10^{-4} N) to the robot so that the induced normal force from the substrate could be decreased. The average angular velocities about the robot's x-, y- and z-axes in this experiment were 20.4 degree/second, 18.7 degree/second and 47.2 degree/second, respectively. To demonstrate the robot's six-DOF motions within the fluid bulk, the robot

was first levitated to break contact with the substrate before it executed the motions. As it was not within our scope to create a neutrally-buoyant robot, the robot's net force along the gravitational direction was not balanced, and this had caused the robot to sink while each motion was executed (SI Video S1). However, as the robot was immersed within a viscous Newtonian fluid in this experiment (glycerol with a viscosity of 648 cSt), it could sink slow enough for each motion to be observed well. In this experiment, the average angular velocities about the robot's x-, y- and z-axes were 73.3 degree/second, 70.5 degree/second and 26.2 degree/second, respectively. Our optimal robot was also able to rotate at a maximum angular velocity of 173 degree/second about its sixth-DOF axis when it was immersed in paraffin oil (viscosity between 100 to 145 cSt) (SI Video S1). The highest sixth-DOF angular velocity of our optimal MMR was therefore 43.25 folds faster than the robot reported by Petruska (52), which had a maximum speed of 4 degree/second about the sixth-DOF axis. In this experiment, an upward magnetic force was applied to the robot until it established good contact with the oil-air interface. This was to prevent the robot from sinking as it was rotating about its sixth-DOF axis. In general, the highest sixth-DOF angular velocity of our optimal robot was dependent on the maximum sixth-DOF torque that our magnetic actuation system could provide to the robot as well as the viscous torque exerted on the robot by the surrounding fluids and fluid-air interface. Hence, it would be possible to further improve the highest sixth-DOF angular velocities of our optimal robots by enhancing the capabilities of our electromagnetic coil system and optimizing the robots' geometries so that they could become more efficient from an aerodynamical perspective.

The ability to precisely control the robot's sixth-DOF angular displacement had also been evaluated experimentally. Using the proposed actuation method, we demonstrated that the optimal six-DOF robot was able to rotate to several selected angular displacements precisely (SI Video S2 and Fig. 2D). This experiment was conducted by sequentially making the selected angular displacements into minimum potential energy configurations, so that a restoring sixth-DOF torque could self-align the robot's sixth-DOF angular displacement to the desired angle. While we had only selected six angular displacements for this proof-of-concept demonstration, these experimental results had nonetheless

suggested that the proposed actuation method was indeed able to precisely control the optimal robot's sixth-DOF angular displacement. Because our optimal MMR was able to perform full six-DOF motions reliably and achieve high sixth-DOF angular velocities (173 degree/second) when they were under precise orientation control (SI Videos S1–2), it showed significant improvements over existing six-DOF MMRs (49-52).

To illustrate the capabilities of our proposed optimal six-DOF MMRs, additional experiments were conducted to evaluate their mobility, and ability to perform small-scale robotic assembly tasks. The mobility of our optimal rigid MMR was demonstrated via making the robot overcome a series of synthetic obstacles (Fig. 3). To highlight the importance of the sixth-DOF motion in this experiment, we had made the rigid robot's geometry to be more asymmetry about its sixth-DOF axis by changing the shape of the auxiliary magnet into a 3D trapezium (Fig. 3A). The obstacles were two parallel walls that were designed to have an opening for the robot to move through (Fig. 3A); otherwise the walls would be impassable for the robot. However, to move through each opening, the robot would have to adjust its orientation about two axes. Specifically, the opening of the first wall could only be passed through if the robot could precisely rotate θ and β to $-90°$ and $45°$, respectively (Fig. 1D and Fig. 3B(i)). Similarly, the opening of the second wall could only be passed through if the robot could precisely rotate θ and α to $-90°$ and $30°$, respectively (Fig. 1D and Fig. 3B(ii)). For the robot to successfully pass through these openings, it also had to maintain the required angular displacements during translation by magnetic-gradient pulling forces. This implies that it was essential for the robot to be able to implement precise orientation control and execute its full six-DOF in a controlled manner in order to pass through these two wall openings (assuming the robots had rigid bodies and the wall openings were similar in size with the robots). As demonstrated, our optimal robot was able to negotiate across the walls easily (SI Video S3 and Fig. 3C). The displayed dexterity was therefore unprecedented as existing rigid miniature robots would not be able to overcome such obstacles. This is because existing rigid miniature robots were either unable to precisely control their sixth-DOF angular displacement (e.g., (29, 30, 49-51, 56)), or it would be challenging to apply desired magnetic forces on these MMRs when they were under precise orientation control (52).

To further highlight the dexterity of our optimal robots, we constructed a six-DOF jellyfish-like robot that could propel itself via a soft-bodied swimming locomotion. This robot had a main component, a pair of soft tentacles, and a light head that made the overall body more neutrally-buoyant (Fig. 4A). By endowing the tentacles with the magnetization profile shown in Fig. 4A, the tentacles could deform into either an "u"- or "n"-shaped configuration through controlling the sign and magnitude of the magnetic field along the sixth-DOF axis (Fig. 4B(i)-(ii)). Based on this shape-changing mechanism, we could enable the robot to swim against gravity by continuously alternating the configurations of the tentacles (SI Video S4). As the robot was swimming in water at a Reynolds number of around 77 (SI section S4B), there were sufficient inertia effects for this time-symmetrical but speed-asymmetrical gait to generate a net propulsion. When the tentacles deformed, they could also provide a net magnetic moment ($\vec{m}$) for the robot. Hence, similar to existing five-DOF jellyfish-like robots (38, 39, 67, 68), our robot could also dictate the propulsion direction by controlling the two axes of angular displacements of its $\vec{m}$ (Fig. 4B(iii), SI Video S4 and SI section S4B).

In contrast to existing five-DOF jellyfish-like robots (38, 39, 67, 68), the unique advantage of our optimal six-DOF robot was that it could control its rotation about the sixth-DOF axis (SI Video S4). Due to this enhanced dexterity, our six-DOF jellyfish-like robot was able to overcome barriers that were impassable by their traditional five-DOF counterparts (38, 39, 67, 68). For instance, here we created a rigid, levelled barrier that had one rectangular opening for the robot to pass through (Fig. 4C(i)). To highlight the importance of the sixth-DOF rotation, we had attached a rigid "NTU"-logo to the robot's head so that its body could become more asymmetric about this axis. Together with the logo, the robot had an "X"-shaped configuration from the top view (Fig. 4C(ii)). Since this configuration was different from the opening's shape, the robot could only overcome this barrier by precisely controlling its sixth-DOF angular displacements to sequentially permit the logo and its body to pass through the opening (Fig. 4D). In the experiment (SI Video S5), the robot was first commanded to swim towards the barrier opening via controlling its two axes of angular displacements to dictate the propulsion direction. To allow the logo to fit and negotiate across the opening, we adjusted the robot's sixth-DOF angular displacement (θ)

from an arbitrary angle to 0° (Fig. 4D(i)). After the logo had passed through (Fig. 4D(ii)), the robot then changed θ from 0° to 90° so that sufficient room could also be created for its body to swim across the opening and thus overcoming this barrier (Fig. 4D(iii)-(iv)). While existing five-DOF jellyfish-like robots could potentially also navigate towards the barrier opening (38, 39, 67, 68), they would lack the sixth-DOF dexterity to negotiate the robot's "X"-shaped configuration across this rectangular opening. The displayed agility of this jellyfish-like robot therefore suggested that the proposed six-DOF technology could also significantly enhance the dexterity of soft-bodied locomotion, and this would be a highly desirable ability for potential biomedical applications (39). In the future, we would aim to implement precise sixth-DOF orientation control for other soft-bodied locomotion such as walking, crawling and jumping (39).

In order to perform 3D, small-scale robotic assembly tasks, we had replaced the auxiliary magnet of the robot in Fig. 1A with a soft-bodied magnetic gripper that had a similar mechanical structure to the grippers reported by Diller et al. (10) (SI section S4C). By bonding this gripper to the main component, this actuator would be able to produce a strong restoring torque about its sixth-DOF axis. To facilitate our subsequent discussions, we would refer to this actuator as the six-DOF soft gripper. In addition to delivering rigid-body motions, the six-DOF soft gripper could also be deformed to produce a gripping motion when we controlled the magnitude of the magnetic field along the robot's net magnetic moment (Fig. 5A(i)). The six-DOF soft gripper could grab more tightly when we increased the magnitude of the magnetic field, and by adjusting the magnitude of the magnetic field, we could make the six-DOF soft gripper grab an object firmly and also release it easily upon command. To position the six-DOF soft gripper more precisely, we could translate it by making it perform stick-slip types of locomotion.

Using the six-DOF soft gripper, we demonstrated that the proposed six-DOF MMRs would be especially beneficial for small-scale robotic assemblies. To benchmark the performance of our six-DOF soft gripper, we commanded it to build a 3D four-bar linkage device (Fig. 5A(ii)) similar to the one shown by Diller et al. (10). While there exist other small-scale robotic assemblies in the literature (e.g., (11, 20, 22, 57-60)), the assembly of a 3D, four-

bar linkage device was selected as a benchmark because it was one of the most complicated millimeter-scale robotic assembly tasks among them.

By controlling the gripper trajectory via a human operator, our six-DOF soft gripper could assemble the four-bar linkage device in 4 minutes 54 seconds (Fig. 5B and SI Video S6). This assembling speed was 20 folds quicker than the previous five-DOF gripper, which required 98 minutes for a human operator to complete (10). While it would be difficult to quantify the enhancements in speed due to the skill difference of the human operators, the key factor in this speed difference was determined by whether the grippers were able to precisely control their sixth-DOF angular displacement. In comparison, the previous five-DOF gripper had a major disadvantage because it had to repeatedly grab and release the four-bar linkage components in different orientations, so as to account for its lack of control over the sixth-DOF rotational axis (10). Conversely, as our six-DOF soft gripper had full control over its six-DOF motions, it could easily orientate and position the four-bar linkage components into their correct destinations, thereby significantly reducing the assembly time. The enhancement in capability of our six-DOF soft gripper over the previous five-DOF gripper (10), had therefore highlighted the importance of having six-DOF actuation for small-scale soft robots. As a potential future work, we aim to further enhance the assembly speed via automating the gripper trajectories. It will be highly advantageous to increase the manipulation capabilities of small-scale, untethered actuators as they can potentially facilitate unprecedented manipulations in lab-on-chip applications, materials science and biology (10, 11, 20, 58, 60).

Discussion

It is noteworthy that the six-DOF MMRs of Petruska (52) will not be able to produce sixth-DOF torques based on our proposed quasi-static actuation method. This is because their magnetization profile is uniform, resulting their **D** matrix to be not full ranked (49, 50). In general, such robots can still achieve six-DOF via dynamic magnetic fields (52). However, such actuation methods will have restrictions on the robots' achievable sixth-DOF angular velocities (4 degree/second) and it is also difficult to apply desired magnetic forces on these MMRs when they are under precise orientation control.

Because the fabrication process in Fig. 1B(vi) was done via mechanical cutting, we had only demonstrated the construction of millimeter-scale robots here as a proof-of-concept. Smaller robots that have hundred microns length-scales, however, can be constructed if the cut-out process in Fig. 1B(vi) is implemented via the laser machining techniques shown in (38, 39), and this can be explored as a future work. Nevertheless, because the sixth-DOF torque scales with L^4 (L represents the robot characteristic length) while the other magnetic torques scales with L^3 (SI section S1B), it is inherent that the sixth-DOF torque would be weaker than the other magnetic torques at smaller scales (69). A potential limitation of the proposed fabrication method is that our main component can only be constructed by hyperelastic materials since its quadrants have to undergo a large deformation during the magnetization process (Fig. 1B(i)-(iii)). However, as the selected material of our main component is a common magnetic polymer composite for constructing miniature robots (38, 39) (Materials section A), the fabricated optimal robots can potentially still be applied across a wide range of applications.

While the optimal main component in Fig. 1A(ii) has never been constructed in the literature, there exists more than one method to fabricate this component. For example, our proposed fabrication process can be modified by replacing the molded quadrants with molded semi-circles (Fig. S4A). In this case, as long as the molded semi-circles can be deformed into full circles before they are magnetized, the main component in Fig. 1A(ii) can similarly be constructed via bonding two of such magnetized semi-circles together (Fig. S4B-E). However, as it is more challenging to deform semi-circles into full circles than to deform quadrants into semi-circles, it will be easier to implement the fabrication method shown in Fig. 1B than on this modified method.

A potential limitation of the actuation method is that there may exist multiple minimum potential energy configurations for a given set of actuating signals, and this will make the robot's final configuration dependent on its previous orientation. To prevent the robot from rotating into an unwanted minimum potential energy configuration, the angular trajectories of the robot can be broken down into more points to reduce the deviation between two sequential orientations. By reducing the deviations, it will be easier to rotate the robot into

its desired configuration (38). Using this approach, our experimental results indicate that this potential limitation can be mitigated, and we are able to implement precise orientation control for our optimal six-DOF MMRs. A detailed analysis to study the effects of having multiple minimum potential energy configurations, however, will be beyond the scope of this work and such studies can be explored as a potential future work.

Equation (6) suggests that the magnitude of the second null space vector will approach infinity when θ satisfied the following condition: $d_{15}\cos 2\theta - d_{14}\sin 2\theta = 0$. Those angles of θ that satisfied such a condition are also known as the singularity angles. The values of the singularity angles, however, can be altered via changing the format of the second null space vector (see SI section S3C). By alternating the format of the second null space vector according to the range of θ, the singularity issues can be moderated because the robot will be able to avoid all the singularity points as it undergoes an angular trajectory.

Using our proposed actuation method, the sixth-DOF restoring torque of the robots will have a valid working range. In general, this working range will be dependent on the robots' geometry and magnetization profile. Here we have determined that the working range of our optimal robots is $180°$. As long as the robots' sixth-DOF angular displacement is within $\pm 90°$ from their desired angle (θ), they will experience the required sixth-DOF restoring torque to eventually be rotated into this desired orientation (SI section S3B).

As our optimal MMRs are not neutrally-buoyant, they may sink in the fluid bulk when their six-DOF motions are executed (as shown in SI Video S1). A potential method to mitigate this issue is to implement closed-loop position control on these actuators with visual feedback. Using such control methods, these MMRs may potentially be able to settle within the fluid bulk and not sink or float up to the air-fluid interface. For lab-on-chip applications, such visual feedback can be implemented via standard cameras (20, 22, 30). Conversely, biomedical related applications may require ultrasound imaging techniques to obtain visual feedback of the six-DOF MMRs when they are operating in the human body (39). Ultrasound imaging techniques have shown to be promising for biomedical applications as previous preliminary works suggest that such visual feedback methods have negligible

interferences with the actuation of MMRs (39). In the future, we aim to investigate such closed-loop control methods for our optimal six-DOF MMRs.

Conclusion

This work proposes a fabrication method and an actuation method that can resolve the critical challenges of six-DOF MMRs. A notable advantage of our fabrication method is that it can create optimal MMRs which are able to produce 51–297 folds larger sixth-DOF torque than existing similar actuators, while ensuring that their traditional five-DOF actuation is not compromised. Using the proposed actuation and fabrication methods, we had created various optimal six-DOF MMRs that were able to exhibit unprecedented dexterity and manipulation capabilities. The key performance indexes of our optimal robots are summarized in Tables 1–3, and these indexes are compared against all the existing small-scale, magnetic actuators with six-DOF as well as selected ones with five-DOF. We envision that this work can inspire future small-scale robots to become significantly more capable and functional, and such untethered actuators can be used across a broad range of applications in robotics, materials science and biomedicine.

Table 1. Key performance indexes of small-scale, magnetic actuators. The performances of our optimal robots are compared against all the existing small-scale, magnetic actuators with six-DOF as well as selected ones with five-DOF.

	DOF	**Able to perform three-axes of precise orientation control**	**Able to execute soft-bodied functionalities**
Cabanach et al. (65) Xu et al. (54) Huang et al. (66) Hu et al. (39) Lum et al. (38)	Five	No	Yes, except for the actuators reported by Cabanach et al. (65)
Petruska (52)	Six	Yes, highest sixth-DOF angular velocity: 4 degree/second. Under precise orientation control, it is challenging to apply desired magnetic forces on these MMRs.	No
Giltinan and Sitti (51)	Six	No	No
Diller et al. (49, 50)	Six	No	No
This Work*	Six	Yes, highest sixth-DOF angular velocity: 173 degree/second. Able to execute full six-DOF motions under precise orientation control.	Yes

Table 2. Comparison between all existing miniature jellyfish-like robots, which can be magnetically actuated to execute a reciprocal swimming locomotion.

	DOF	**Sufficient dexterity to negotiate across the barrier in Fig. 4D**
Ren et al. (67)	Five	No
Ren et al. (68)	Five	No
Hu et al. (39)	Five	No
Lum et al. (38)	Five	No
This Work*	Six	Yes

Table 3. Comparison between different miniature soft grippers, which can be magnetically actuated to perform assembly tasks.

	DOF	Able to complete the 3D assembly in Fig. 5
Goudu et al. (63) Xu et al. (54) Hu et al. (39)	Five	Not demonstrated, restricted to 2D assembly tasks
Diller and Sitti (10)	Five	Yes, required 98 minutes to complete the 3D assembly
This Work*	Six	Yes, required 4 minutes 54 seconds to complete the 3D assembly

Methods

A. Materials

Except for the jellyfish-like robot and six-DOF soft gripper (SI section S4B-C), the mass ratio between the polymer matrix and magnetic particles was always 1:1 for all the components. The magnetization magnitude for this mass ratio, when the magnetizing field was 1.1 T, was measured by a vibrating-sample magnetometer to be 55900 ± 2620 A/m (five measurements). The highest concentration of NdFeB particles that we could embed into the main component was experimentally evaluated to have the following polymer to particles mass ratio: 1:4. While quadrants with this mass ratio could still undergo the required deformation specified in Fig. 1B(i)-(ii), it was difficult to further increase the amount of NdFeB particles because it would be hard to mix the particles uniformly into the polymer matrix.

To adhesively bond the quadrants together, good contact was established at their connecting surfaces after these surfaces were coated with a thin layer of liquid Ecoflex 00-10. Once the liquid Ecoflex 00-10 cured, the quadrants would be strongly bonded together. Unless specified otherwise, our main components in the experiments were always constructed to have a 3 mm diameter and a 1 mm out-of-plane thickness. The auxiliary magnet, jellyfish-like robot and the soft gripper were bonded to the main component via the following adhesive: Loctite 495.

B. Experimental setup

A custom-made electromagnetic coil system, which is of similar design to the one presented in (30), is used to generate the actuating magnetic fields for the six-DOF robots (Fig. S1). By controlling the electrical current in the coils, we are able to generate the desired $\vec{B}$ and $\vec{B}_{\text{grad}}$ for our optimal six-DOF robots. The maximum producible $|\vec{B}|$ and its

spatial-gradients of this system are 12 mT and 0.26 T/m, respectively, and these values dictate the maximum allowable k_1 and k_2 in Eq. (6). At the center of this system, there is an inner chamber, which has a workspace of 16 mm × 16 mm × 16 mm that can produce a 90% homogeneous field. Unless specified otherwise, the experiments were always conducted by immersing the robots in a medium of paraffin oil (viscosity: 100-145 cSt). For all the experiments, the robots were always placed in the workspace of the coil system (Fig. S1). The utilized magnetic actuating signals in our experiments, with respect to the global reference frame, can be found in Fig.s S8-S23.

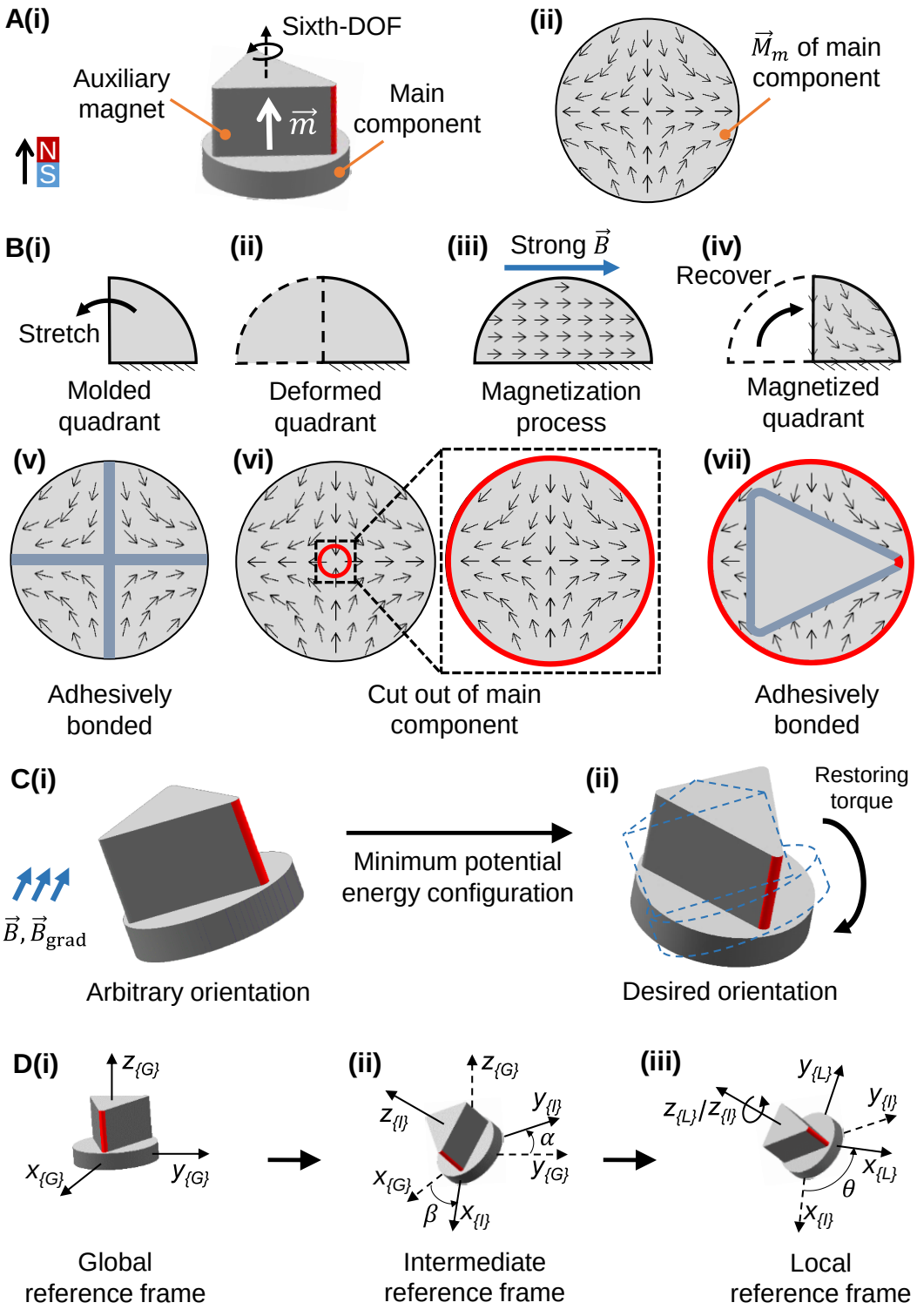
A(i)
Sixth-DOF
Auxiliary magnet
Main component
$\vec{m}$
N
S
(ii)
$\vec{M}_m$ of main component
B(i)
Stretch
Molded quadrant
(ii)
Deformed quadrant
(iii)
Strong $\vec{B}$
Magnetization process
(iv)
Recover
Magnetized quadrant
(v)
Adhesively bonded
(vi)
Cut out of main component
(vii)
Adhesively bonded
C(i)
$\vec{B}, \vec{B}_{\text{grad}}$
Arbitrary orientation
Minimum potential energy configuration
(ii)
Restoring torque
Desired orientation
D(i)
$z_{\{G\}}$
$x_{\{G\}}$
$y_{\{G\}}$
Global reference frame
(ii)
$z_{\{G\}}$
$z_{\{I\}}$
$y_{\{I\}}$
α
$y_{\{G\}}$
$x_{\{G\}}$
β
$x_{\{I\}}$
Intermediate reference frame
(iii)
$y_{\{L\}}$
$z_{\{L\}}/z_{\{I\}}$
$y_{\{I\}}$
$x_{\{L\}}$
θ
$x_{\{I\}}$
Local reference frame

Fig. 1. A conceptual illustration for the proposed fabrication and actuation methods. (A) The proposed optimal six-DOF MMR. (i) The robot has a uniformly magnetized auxiliary magnet and a main component that has a non-uniform magnetization profile. The robot's sixth-DOF axis is parallel to its net magnetic moment ($\vec{m}$). To have a better reference on the robot's sixth-DOF angular displacement, one of the edges of the auxiliary magnet is highlighted in red. (ii) The non-uniform magnetization profile $\left(\vec{M}_m\right)$ of the main component. (B) The proposed fabrication steps. (i) Once a quadrant is molded, it will undergo a rotational deformation such that it can be stretched into a semi-circle configuration as shown in (ii). (iii) The deformed quadrant will be magnetized by a strong, uniform magnetic field. (iv) Once the quadrant recovers back to its original shape, it will possess the optimal magnetization profile. (v-vi) Four quadrants are adhesively bonded together before a smaller main component is cut out from the center. The greyish blue lines in (v) represent the adhesive bonding process. (vii) The auxiliary magnet and main component are adhesively bonded together to form the optimal robot. (C) By making the desired orientation into a minimum potential energy configuration, a six-DOF MMR with non-uniform magnetization profile will constantly experience a restoring torque until it reaches the desired orientation. (D) The three reference frames required for understanding and implementing the proposed actuation method. The global, intermediate and local reference frames of the robot are shown in (i), (ii) and (iii), respectively. Before the robot rotates, its local reference frame in (iii) coincides with the global reference frame.

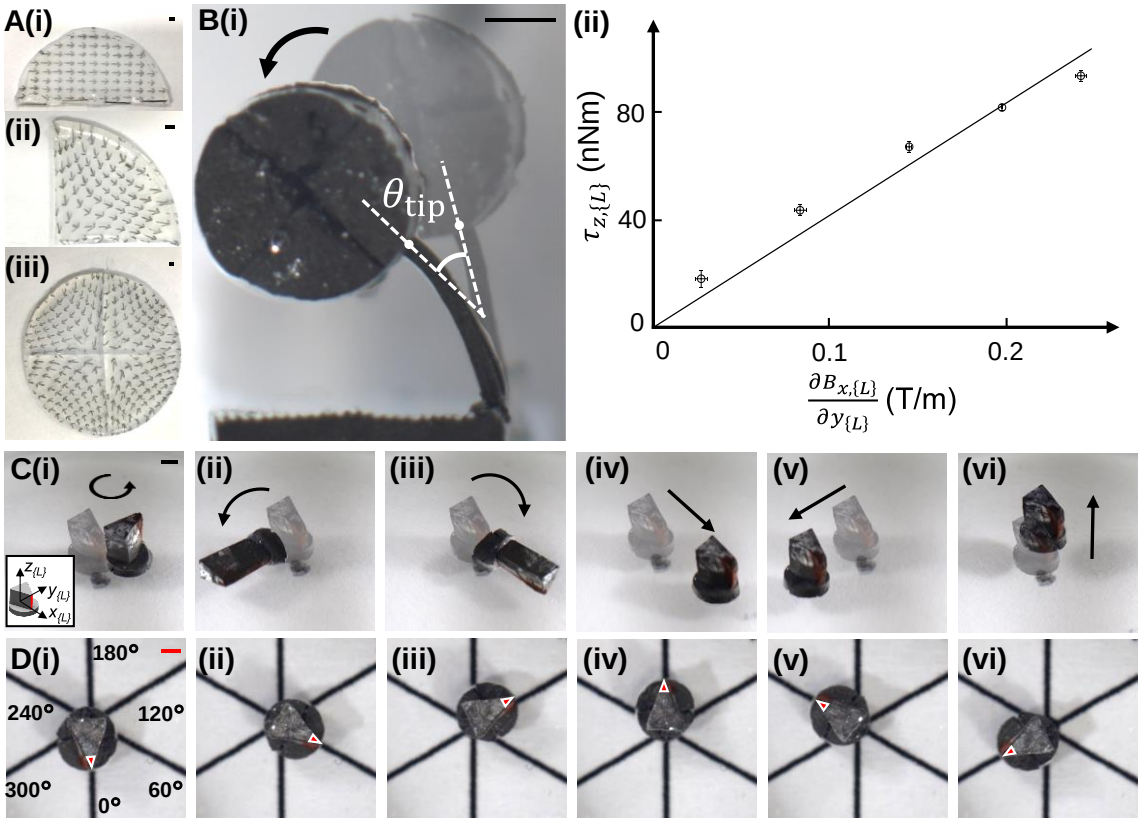
A(i)
(ii)
(iii)
B(i)
θ_{tip}
(ii)
80
40
0
0
0.1
0.2
$\tau_{z,\{L\}}$ (nNm)
$\frac{\partial B_{x,\{L\}}}{\partial y_{\{L\}}}$ (T/m)
C(i)
(ii)
(iii)
(iv)
(v)
(vi)
$z_{\{L\}}$
$y_{\{L\}}$
$x_{\{L\}}$
D(i)
180°
240°
120°
300°
60°
0°
(ii)
(iii)
(iv)
(v)
(vi)

Fig. 2. Experimental results for the optimal six-DOF MMR in Fig. 1A. (A) A centimeter-scale main component was constructed based on the proposed fabrication method (Fig. 1B(i-v)). (i)-(ii) The magnetization process in Fig. 1B(iii) was simulated by drawing horizontal arrows on the main component. (iii) The obtained magnetization profile of the main component was shown to be similar to the one illustrated in Fig. 1A(ii). (B) Evaluating the producible sixth-DOF torque of a main component that had a 3 mm diameter and a 1 mm out-of-plane thickness. (i) The main component was attached to the free-end of a fix-free beam. When the sixth-DOF torque was applied on the main component, the deformation angle at the beam's free-end, θ_{tip}, would be measured accordingly. To measure θ_{tip}, we compared the tangent lines at the beam's free-end before and after the deformation. (ii) The experimental plot of the measured $\tau_{Z,\{L\}}$ against the applied magnetic actuating signals $\frac{\partial B_{x,\{L\}}}{\partial y_{\{L\}}}$, and the error bars represented the standard deviation of each data point. The gradient of the best fit line was computed to be 4.20×10^{-7} Nm^2/T and it represented the normalized sixth-DOF torque of the main component. (C) Demonstrating the robot's six-DOF rigid-body motions on a passive substrate, where the robot's local reference frame was shown in the inset of (i). (i)-(iii) Rotation about the robot's $z_{\{L\}}$-, $x_{\{L\}}$- and $y_{\{L\}}$-axes, respectively. The sixth-DOF rotation was illustrated in (i). (iv)-(vi) Translation along the robot's $x_{\{L\}}$-, $y_{\{L\}}$- and $z_{\{L\}}$-axes, respectively. (D) Using the proposed actuation method to implement precise sixth-DOF orientation control for the robot. By sequentially making the desired sixth-DOF angular displacements (0˚, 60˚, 120˚, 180˚, 240˚, and 300˚) into minimum potential energy configurations, the robot was shown to be able to self-align to these angles in a precise and reliable manner. We highlighted the tip of the auxiliary magnet to better illustrate the robot's sixth-DOF angular displacement. Scale bars: 1 mm.

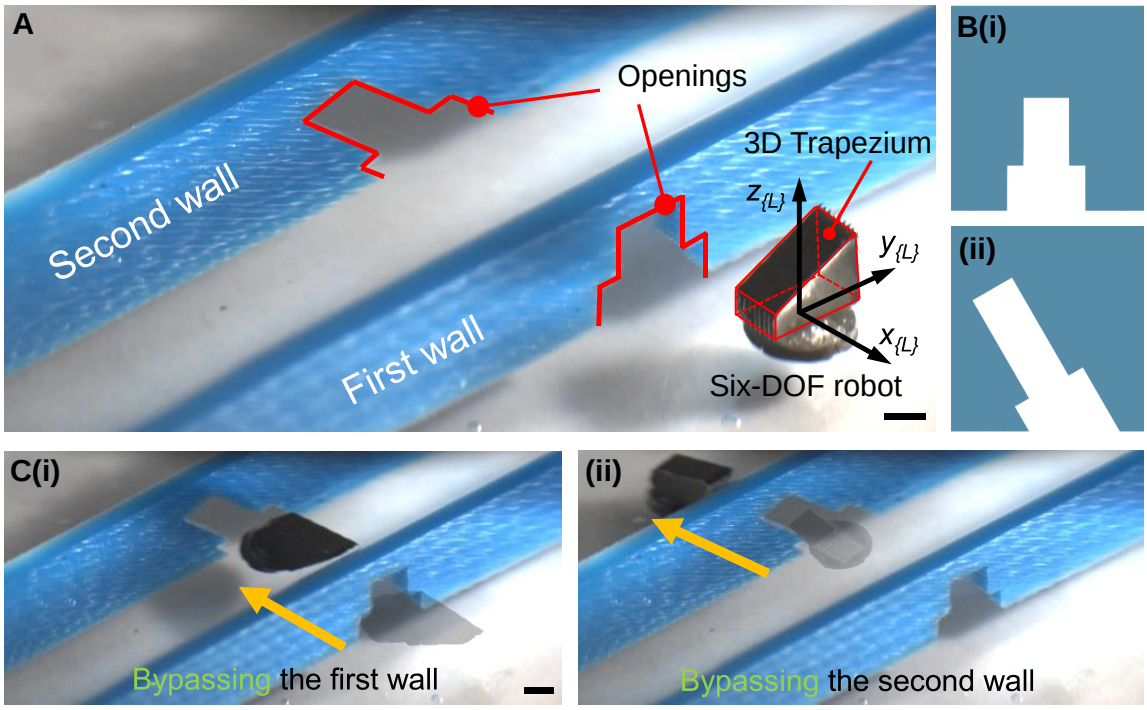

Fig. 3. Negotiating the robot across two rigid walls. (A) In this experiment, the robot had to perform precise orientation control and full six-DOF actuation to pass through the openings of both walls. Before the experiment began, the global and local reference frames coincided. (B) The front view of the wall openings; the first and second wall openings are shown in (i) and (ii), respectively. (C) Snapshots from SI Video S3; (i) showed that the robot could only negotiate through the first wall if it could precisely rotate θ and β to $-90°$ and $45°$, respectively. Similarly, (ii) showed that the robot could only pass through the second wall if it could rotate θ and α to $-90°$ and $30°$, respectively. Scale bars: 1 mm.

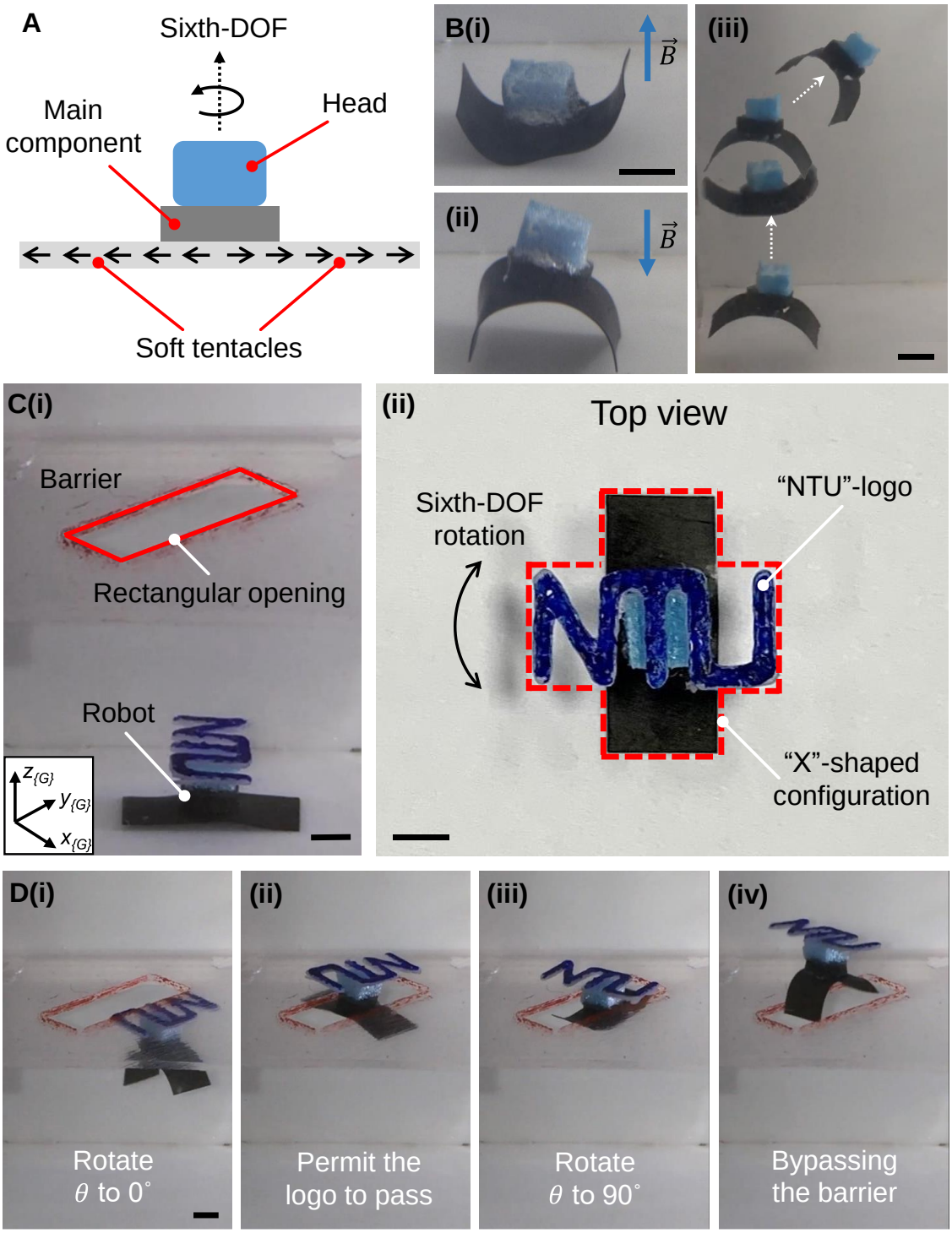
A
Sixth-DOF
Main component
Head
Soft tentacles
B(i)
(ii)
(iii)
C(i)
Barrier
Rectangular opening
Robot
(ii)
Top view
Sixth-DOF rotation
"NTU"-logo
"X"-shaped configuration
D(i)
Rotate θ to 0˚
(ii)
Permit the logo to pass
(iii)
Rotate θ to 90˚
(iv)
Bypassing the barrier

Fig. 4. A six-DOF jellyfish-like robot that can propel itself via a soft-bodied swimming locomotion. (A) This robot is composed by a head, a main component and a pair of soft tentacles. The magnetization profile of the tentacles is symmetrical about the robot's sixth-DOF axis. (B) (i-ii) The robot would assume either a "u"- or "n"-shaped configuration when $\vec{B}$ was applied along its sixth-DOF axis. (iii) By controlling the direction of $\vec{B}$, we could control the propulsion direction of the robot. (C) The setup for the experiment in SI Video S5. (i) The initial position and orientation of the robot before it began the experiment. (ii) The top view of the robot after it was attached to a rigid "NTU"-logo. Together with the logo, the robot would have an "X"-shaped configuration. (D) Snapshots from SI Video S5. This experiment aimed to evaluate the robot's dexterity by making it swim past the rectangular barrier opening with its "X"-shaped configuration. (i-ii) The robot rotated its sixth-DOF angle to 0° so that the logo could be permitted to pass through the barrier opening. (iii-iv) The robot then rotated its sixth-DOF angle to 90° to permit its remaining body to negotiate across the opening, thereby bypassing this barrier. Scale bars: 2 mm.

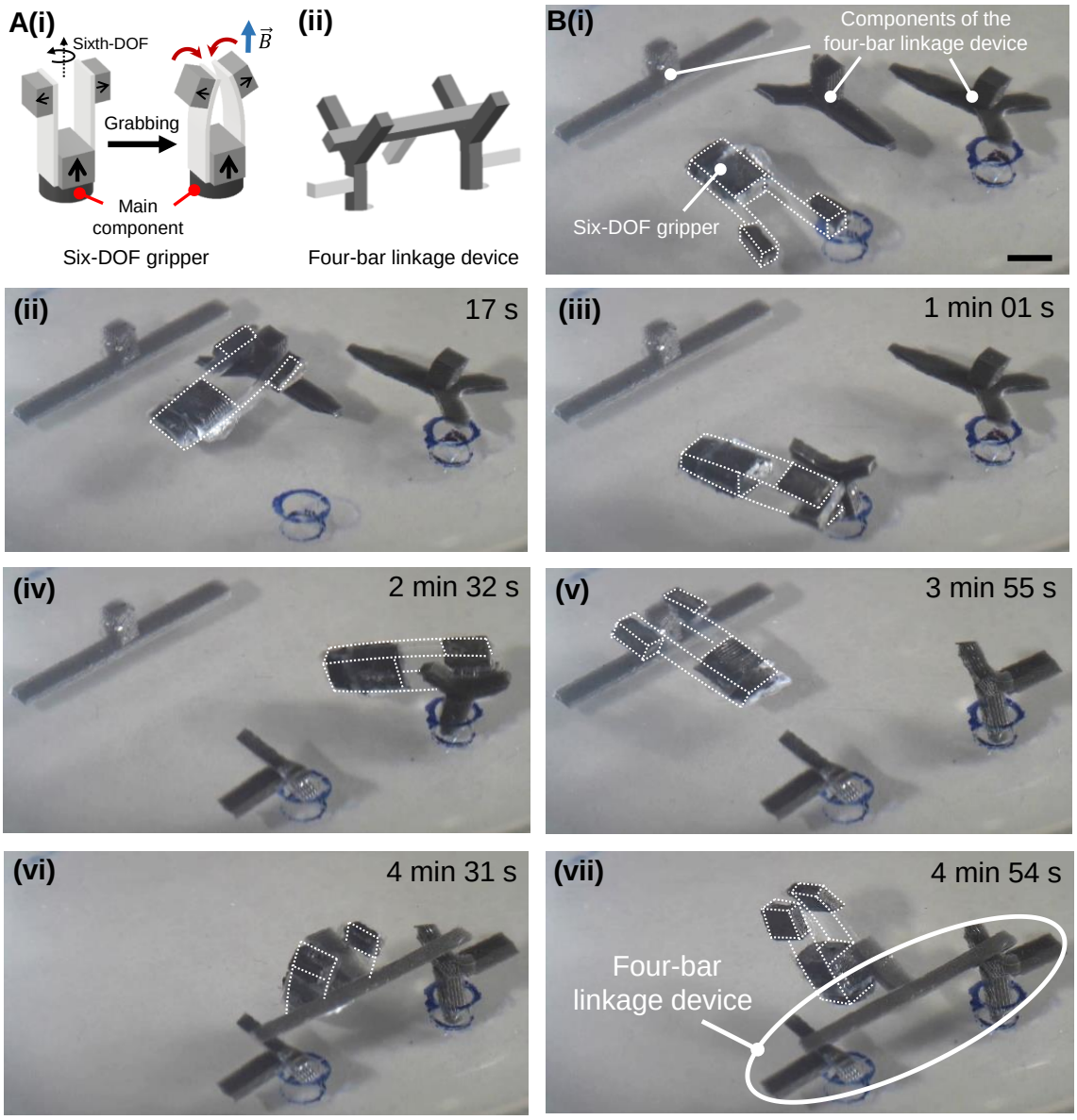

Fig. 5. Robotic assembly of a 3D four-bar linkage device. (A) (i) A six-DOF soft gripper is created by replacing the auxiliary magnet of the robot with a gripping mechanism. By controlling the magnitude of $\vec{B}$ along the robot's net magnetic moment, the six-DOF soft gripper can produce a grabbing motion. (ii) The desired four-bar linkage device that the robot is commanded to build. (B) Snapshots from SI Video S6 to illustrate the assembly process. To increase the clarity of this figure, the six-DOF soft gripper was outlined with dotted white lines. Scale bar: 2 mm.

References

1. M. Sitti *et al.*, Biomedical applications of untethered mobile milli/microrobots. *Proceedings of the IEEE* **103**, pp 205-224. (2015).
2. B. J. Nelson, I. K. Kaliakatsos, J. J. Abbott, Microrobots for minimally invasive medicine. *Annual Review of Biomedical Engineering* **12**, pp 55-85. (2010).
3. M. Sitti, Miniature soft robots—road to the clinic. *Nature Reviews Materials* **3**, p 74. (2018).
4. S. Palagi *et al.*, Structured light enables biomimetic swimming and versatile locomotion of photoresponsive soft microrobots. *Nature Materials* **15**, pp 647-653. (2016).
5. M. Sitti, Voyage of the microrobots. *Nature* **458**, pp 1121-1122. (2009).
6. O. Felfoul *et al.*, Magneto-aerotactic bacteria deliver drug-containing nanoliposomes to tumour hypoxic regions. *Nature Nanotechnology* **11**, pp 941-947. (2016).
7. C. S. X. Ng, M. W. M. Tan, C. Xu, Z. Yang, P. S. Lee, G. Z. Lum, Locomotion of miniature soft robots. *Advanced Materials*, DOI: 10.1002/adma.202003558, p 2003558. (2020).
8. Z. Wu *et al.*, A swarm of slippery micropropellers penetrates the vitreous body of the eye. *Science Advances* **4**, p eaat4388. (2018).
9. L. Hines, K. Petersen, G. Z. Lum, M. Sitti, Soft actuators for small‐scale robotics. *Advanced Materials* **29**, p 1603483. (2017).
10. E. Diller, M. Sitti, Three‐dimensional programmable assembly by untethered magnetic robotic micro‐grippers. *Advanced Functional Materials* **24**, pp 4397-4404. (2014).
11. S. Tasoglu, E. Diller, S. Guven, M. Sitti, U. Demirci, Untethered micro-robotic coding of three-dimensional material composition. *Nature Communications* **5**, pp 1-9. (2014).
12. H. Ceylan, J. Giltinan, K. Kozielski, M. Sitti, Mobile microrobots for bioengineering applications. *Lab on a Chip* **17**, pp 1705-1724. (2017).
13. Z. Ye, M. Sitti, Dynamic trapping and two-dimensional transport of swimming microorganisms using a rotating magnetic microrobot. *Lab on a Chip* **14**, pp 2177-2182. (2014).
14. W. Hu, K. S. Ishii, A. T. Ohta, Micro-assembly using optically controlled bubble microrobots. *Applied Physics Letters* **99**, p 094103. (2011).
15. V. Magdanz, S. Sanchez, O. G. Schmidt, Development of a sperm‐flagella driven micro‐bio‐robot. *Advanced Materials* **25**, pp 6581-6588. (2013).
16. S. Kim *et al.*, Fabrication and characterization of magnetic microrobots for three‐dimensional cell culture and targeted transportation. *Advanced Materials* **25**, pp 5863-5868. (2013).
17. M. S. Sakar, E. B. Steager, D. H. Kim, M. J. Kim, G. J. Pappas, V. Kumar, Single cell manipulation using ferromagnetic composite microtransporters. *Applied Physics Letters* **96**, p 043705. (2010).
18. X. Dong *et al.*, Bioinspired cilia arrays with programmable nonreciprocal motion and metachronal coordination. *Science Advances* **6**, p eabc9323. (2020).
19. H. Gu *et al.*, Magnetic cilia carpets with programmable metachronal waves. *Nature Communications* **11**, p 2637. (2020).
20. S. E. Chung, X. Dong, M. Sitti, Three-dimensional heterogeneous assembly of coded microgels using an untethered mobile microgripper. *Lab on a Chip* **15**, pp 1667-1676. (2015).

21. E. Diller, S. Miyashita, M. Sitti, Remotely addressable magnetic composite micropumps. *RSC Advances* **2**, pp 3850-3856. (2012).
22. X. Dong, M. Sitti, (2017) Planning spin-walking locomotion for automatic grasping of microobjects by an untethered magnetic microgripper. in *2017 IEEE International Conference on Robotics and Automation (ICRA)*, pp 6612-6618.
23. J. Cui *et al.*, Nanomagnetic encoding of shape-morphing micromachines. *Nature* **575**, pp 164-168. (2019).
24. Y. Kim, H. Yuk, R. Zhao, S. A. Chester, X. Zhao, Printing ferromagnetic domains for untethered fast-transforming soft materials. *Nature* **558**, pp 274-279. (2018).
25. L. S. Novelino, Q. Ze, S. Wu, G. H. Paulino, R. Zhao, Untethered control of functional origami microrobots with distributed actuation. *Proceedings of the National Academy of Sciences* **117**, pp 24096-24101. (2020).
26. E. Diller, J. Zhuang, G. Zhan Lum, M. R. Edwards, M. Sitti, Continuously distributed magnetization profile for millimeter-scale elastomeric undulatory swimming. *Applied Physics Letters* **104**, p 174101. (2014).
27. S. Tottori, B. J. Nelson, Controlled propulsion of two‐dimensional microswimmers in a precessing magnetic field. *Small* **14**, p 1800722. (2018).
28. A. W. Mahoney, J. J. Abbott, Five-degree-of-freedom manipulation of an untethered magnetic device in fluid using a single permanent magnet with application in stomach capsule endoscopy. *The International Journal of Robotics Research* **35**, pp 129-147. (2016).
29. S. Tottori, L. Zhang, F. Qiu, K. K. Krawczyk, A. Franco‐Obregón, B. J. Nelson, Magnetic helical micromachines: fabrication, controlled swimming, and cargo transport. *Advanced Materials* **24**, pp 811-816. (2012).
30. M. P. Kummer, J. J. Abbott, B. E. Kratochvil, R. Borer, A. Sengul, B. J. Nelson, OctoMag: An electromagnetic system for 5-DOF wireless micromanipulation. *IEEE Transactions on Robotics* **26**, pp 1006-1017. (2010).
31. D. R. Frutiger, K. Vollmers, B. E. Kratochvil, B. J. Nelson, Small, fast, and under control: wireless resonant magnetic micro-agents. *The International Journal of Robotics Research* **29**, pp 613-636. (2010).
32. L. Zhang, J. J. Abbott, L. Dong, B. E. Kratochvil, D. Bell, B. J. Nelson, Artificial bacterial flagella: fabrication and magnetic control. *Applied Physics Letters* **94**, p 064107. (2009).
33. E. Diller, C. Pawashe, S. Floyd, M. Sitti, Assembly and disassembly of magnetic mobile micro-robots towards deterministic 2-D reconfigurable micro-systems. *The International Journal of Robotics Research* **30**, pp 1667-1680. (2011).
34. E. Diller, S. Floyd, C. Pawashe, M. Sitti, Control of multiple heterogeneous magnetic microrobots in two dimensions on nonspecialized surfaces. *IEEE Transactions on Robotics* **28**, pp 172-182. (2011).
35. P. Vartholomeos, M. R. Akhavan-Sharif, P. E. Dupont, (2012) Motion planning for multiple millimeter-scale magnetic capsules in a fluid environment. in *2012 IEEE International Conference on Robotics and Automation*, pp 1927-1932.
36. S. Miyashita, S. Guitron, S. Li, D. Rus, Robotic metamorphosis by origami exoskeletons. *Science Robotics* **2**, p eaao4369. (2017).
37. T. Qiu *et al.*, Swimming by reciprocal motion at low Reynolds number. *Nature Communications* **5**, pp 1-8. (2014).
38. G. Z. Lum *et al.*, Shape-programmable magnetic soft matter. *Proceedings of the National Academy of Sciences* **113**, pp E6007-E6015. (2016).

39. W. Hu, G. Z. Lum, M. Mastrangeli, M. Sitti, Small-scale soft-bodied robot with multimodal locomotion. *Nature* **554**, pp 81-85. (2018).
40. J. J. Abbott *et al.*, How should microrobots swim? *The International Journal of Robotics Research* **28**, pp 1434-1447. (2009).
41. A. Eqtami, O. Felfoul, P. E. Dupont, (2014) MRI-powered closed-loop control for multiple magnetic capsules. in *2014 IEEE/RSJ International Conference on Intelligent Robots and Systems*, pp 3536-3542.
42. D. Wong, E. B. Steager, V. Kumar, Independent control of identical magnetic robots in a plane. *IEEE Robotics and Automation Letters* **1**, pp 554-561. (2016).
43. E. B. Steager, D. Wong, D. Mishra, R. Weiss, V. Kumar, (2014) Sensors for micro bio robots via synthetic biology. in *2014 IEEE International Conference on Robotics and Automation (ICRA)*, pp 3783-3788.
44. V. Iacovacci, G. Lucarini, L. Ricotti, P. Dario, P. E. Dupont, A. Menciassi, Untethered magnetic millirobot for targeted drug delivery. *Biomedical Microdevices* **17**, p 63. (2015).
45. M. Latulippe, O. Felfoul, P. E. Dupont, S. Martel, Enabling automated magnetic resonance imaging-based targeting assessment during dipole field navigation. *Applied Physics Letters* **108**, p 062403. (2016).
46. M. Latulippe, S. Martel, Evaluation of the potential of dipole field navigation for the targeted delivery of therapeutic agents in a human vascular network. *IEEE Transactions on Magnetics* **54**, pp 1-12. (2018).
47. Y. Kim, G. A. Parada, S. Liu, X. Zhao, Ferromagnetic soft continuum robots. *Science Robotics* **4**, p eaax7329. (2019).
48. Q. Ze *et al.*, Magnetic shape memory polymers with integrated multifunctional shape manipulation. *Advanced Materials* **32**, p 1906657. (2020).
49. E. Diller, J. Giltinan, G. Z. Lum, Z. Ye, M. Sitti, (2014) Six-degrees-of-freedom remote actuation of magnetic microrobots. in *2014 Robotics: Science and Systems*, DOI: 10.15607/RSS.2014.X.013.
50. E. Diller, J. Giltinan, G. Z. Lum, Z. Ye, M. Sitti, Six-degree-of-freedom magnetic actuation for wireless microrobotics. *The International Journal of Robotics Research* **35**, pp 114-128. (2016).
51. J. Giltinan, M. Sitti, Simultaneous six-degree-of-freedom control of a single-body magnetic microrobot. *IEEE Robotics and Automation Letters* **4**, pp 508-514. (2019).
52. A. J. Petruska, Open-loop orientation control using dynamic magnetic fields. *IEEE Robotics and Automation Letters* **5**, pp 5472-5476. (2020).
53. R. Zhao, Y. Kim, S. A. Chester, P. Sharma, X. Zhao, Mechanics of hard-magnetic soft materials. *Journal of the Mechanics and Physics of Solids* **124**, pp 244-263. (2019).
54. T. Xu, J. Zhang, M. Salehizadeh, O. Onaizah, E. Diller, Millimeter-scale flexible robots with programmable three-dimensional magnetization and motions. *Science Robotics* **4**, p eaav4494. (2019).
55. I. S. Khalil *et al.*, Independent actuation of two-tailed microrobots. *IEEE Robotics and Automation Letters* **3**, pp 1703-1710. (2018).
56. I. S. Khalil *et al.*, Mechanical rubbing of blood clots using helical robots under ultrasound guidance. *IEEE Robotics and Automation Letters* **3**, pp 1112-1119. (2018).
57. J. Giltinan, E. Diller, M. Sitti, Programmable assembly of heterogeneous microparts by an untethered mobile capillary microgripper. *Lab on a Chip* **16**, pp 4445-4457. (2016).

58. J. Zhang, M. Salehizadeh, E. Diller, (2018) Parallel pick and place using two independent untethered mobile magnetic microgrippers. in *2018 IEEE International Conference on Robotics and Automation (ICRA)*, pp 123-128.
59. J. Zhang, O. Onaizah, K. Middleton, L. You, E. Diller, Reliable grasping of three-dimensional untethered mobile magnetic microgripper for autonomous pick-and-place. *IEEE Robotics and Automation Letters* **2**, pp 835-840. (2017).
60. Z. Ye, G. Z. Lum, S. Song, S. Rich, M. Sitti, Phase change of gallium enables highly reversible and switchable adhesion. *Advanced Materials* **28**, pp 5088-5092. (2016).
61. V. K. Venkiteswaran, D. K. Tan, S. Misra, Tandem actuation of legged locomotion and grasping manipulation in soft robots using magnetic fields. *Extreme Mechanics Letters* **41**, p 101023. (2020).
62. X. Du *et al.*, Reconfiguration, camouflage, and color‐shifting for bioinspired adaptive hydrogel‐based millirobots. *Advanced Functional Materials* **30**, p 1909202. (2020).
63. S. R. Goudu, I. C. Yasa, X. Hu, H. Ceylan, W. Hu, M. Sitti, Biodegradable untethered magnetic hydrogel milli‐grippers. *Advanced Functional Materials*, p 2004975. (2020).
64. E. Al Khatib, A. Bhattacharjee, P. Razzaghi, L. W. Rogowski, M. J. Kim, Y. Hurmuzlu, Magnetically actuated simple millirobots for complex navigation and modular assembly. *IEEE Robotics and Automation Letters* **5**, pp 2958-2965. (2020).
65. P. Cabanach *et al.*, Zwitterionic 3D‐printed non‐immunogenic stealth microrobots. *Advanced Materials* **32**, p 2003013. (2020).
66. H.-W. Huang, F. E. Uslu, P. Katsamba, E. Lauga, M. S. Sakar, B. J. Nelson, Adaptive locomotion of artificial microswimmers. *Science Advances* **5**, p eaau1532. (2019).
67. Z. Ren, W. Hu, X. Dong, M. Sitti, Multi-functional soft-bodied jellyfish-like swimming. *Nature Communications* **10**, pp 1-12. (2019).
68. Z. Ren, T. Wang, W. Hu, M. Sitti, (2019) A magnetically-actuated untethered jellyfish-inspired soft milliswimmer. in *2019 Robotics: Science and Systems*, DOI: 10.15607/RSS.2019.XV.013.
69. C. R. Thornley, L. N. Pham, J. J. Abbott, Reconsidering six-degree-of-freedom magnetic actuation across scales. *IEEE Robotics and Automation Letters* **4**, pp 2325-2332. (2019).